Topics in Catalysis (2023) 66:1202–1216
https://doi.org/10.1007/s11244-023-01798-4

ORIGINAL PAPER

Thermal Stability and CO Permeability of $[C_4C_1Pyr][NTf_2]$/Pd(111) Model SCILLs: from UHV to Ambient Pressure

Roman Eschenbacher[1] · Simon Trzeciak[2] · Christian Schuschke[1] · Simon Schötz[1] · Chantal Hohner[1] · Dominik Blaumeiser[1] · Dirk Zahn[2] · Tanja Retzer[1] · Jörg Libuda[1]

Accepted: 24 February 2023 / Published online: 1 April 2023

Abstract

Solid catalysts with ionic liquid layers (SCILLs) are heterogeneous catalysts which benefit significantly in terms of selectivity from a thin coating of an ionic liquid (IL). In the present work, we study the interaction of CO with a Pd model SCILL consisting of a 1-butyl-1-methylpyrrolidinium bis(trifluoromethylsulfonyl)-imide ($[C_4C_1Pyr][NTf_2]$) film deposited on Pd(111). We investigate the CO permeability and stability of the IL film via pressure modulation experiments by infrared reflection absorption spectroscopy (IRAS) in ultrahigh vacuum (UHV) and at ambient pressure conditions by time-resolved, temperature-programmed, and polarization-modulated (PM) IRAS experiments. In addition, we performed molecular dynamics (MD) simulations to identify adsorption motifs, their abundance, and the influence of CO. We find a strongly bound IL wetting monolayer (ML) and a potentially dewetting multilayer. Molecular reorientation of the IL at the interface and multilayer dewetting allow for the accumulation of CO at the metal/IL interface. Our results confirm that co-adsorption of CO changes the molecular structure of the IL wetting layer which confirms the importance to study model SCILL systems under in situ conditions.

Roman Eschenbacher, Simon Trzeciak these authors contributed equally to this work.

✉ Jörg Libuda
joerg.libuda@fau.de

[1] Interface Research and Catalysis, ECRC, Friedrich-Alexander-Universität Erlangen-Nürnberg, Egerlandstraße 3, 91058 Erlangen, Germany

[2] Lehrstuhl für Theoretische Chemie, CCC, Friedrich-Alexander-Universität Erlangen-Nürnberg, Nägelsbachstraße 25, 91052 Erlangen, Germany

Graphical abstract

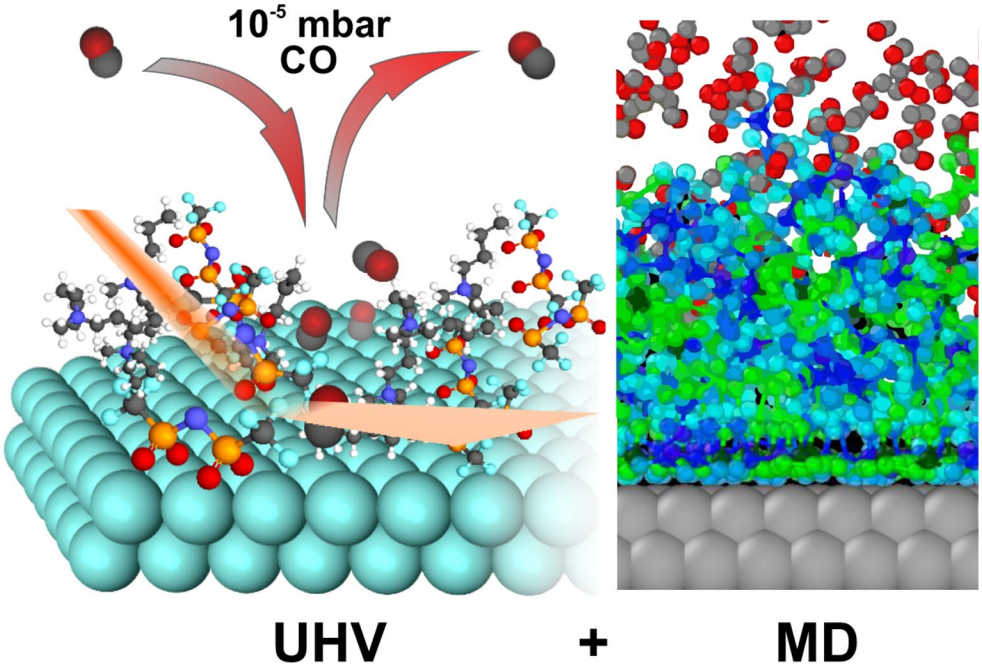

Keywords Ionic Liquids · Infrared Spectroscopy · Molecular Dynamics · SCILL · Permeability · In Situ

1 Introduction

One strategy to improve the selectivity of heterogeneous catalysts relies on ionic liquids (ILs) as catalytic modifiers [1–3]. ILs are low melting salts (by definition with a melting point < 100 °C), which consist of organic cations and anions. Many ILs are liquid even at room temperature (RTILs). Due the large number of possible ion combinations, their physicochemical properties can be adapted in a task-specific fashion [4–8]. In the so-called solid catalyst with ionic liquid layer (SCILL), an IL is applied as a thin coating on a conventional supported catalyst [2, 3, 9–12]. It has been shown that the IL layer strongly improves the selectivity, in particular in case of hydrogenation reactions for which the concept is already applied at industrial scale [11, 13–15].

In SCILL systems, the active metal sites are selectively modified by adsorption of the IL ions [9, 15–17]. To design such systems on a knowledge-driven basis, it is essential to understand this interaction at the microscopic level. Here, surface science experiments in ultrahigh vacuum (UHV) can provide very detailed information [1, 10, 18, 19]. As the vapour pressure of ILs is extremely low, stable IL films can be deposited by physical vapor deposition (PVD) in UHV onto an atomically clean surface [10, 19–22]. In several surface science studies, the wetting behavior and the orientation of IL ions at the solid/liquid interface were investigated [18, 23–26]. Recently, we studied the interaction of 1-butyl-1-methylpyrrolidinium bis(trifluoromethylsulfonyl)-imide ($[C_4C_1Pyr][NTf_2]$) with Pd(111) by infrared reflection absorption spectroscopy (IRAS), molecular dynamics (MD) simulations, and density functional theory (DFT) calculations [27]. We identified the most common binding motifs of the strongly bound $[NTf_2]^-$ anions and showed that the binding motifs change dynamically with the IL coverage.

Other important aspects of SCILL systems are the solubility and diffusion behavior of reactants, intermediates, and products [3, 15–17, 28–30]. On the one hand, it is essential to form IL films which show a strong enough interaction with the active metal to ensure complete wetting of the metal surface, since transport processes in the IL layer control the catalytic activity. On the other hand, the film has to be sufficiently dynamic to allow for permeation of the reactants to the active sites. In this study, we use CO as a probe molecule to test wetting, permeation, and adsorbate dynamics in an $[C_4C_1Pyr][NTf_2]$ layer on Pd(111) [3, 28, 31]. We explored the molecular orientation and interaction mechanisms at the IL/Pd(111) interface by IRAS and polarization modulation (PM) IRAS over a broad pressure range from UHV to ambient conditions. In particular, we tested (i) the influence of preadsorbed CO on the molecular arrangement at the IL/metal interface and (ii) the permeability of IL thin films for CO both under UHV and ambient conditions. We rationalize our results based on Molecular Dynamics

(MD) simulations which allow for quantitative analysis of the preferred adsorption geometries. Our results show that CO permeability is only possible through dewetted IL multilayer areas and intermolecular interactions in the first wetting layer are essential for CO co-adsorption.

2 METHODS

Experimental setup. The IRAS experiments were conducted in a combined UHV IRAS system. The setup (base pressure of 1×10^{-10} mbar) features various preparation and characterization tools which are necessary to prepare and investigate thin films. The setup is equipped with a vacuum Fourier-transform infrared (FTIR) spectrometer (Bruker Vertex 80v). A detailed description of the setup is given in the literature [32].

Preparation of the Pd(111) single crystal. The Pd(111) single crystal (MaTecK) was cleaned by several cycles of Ar^+ sputtering (1 keV, 300 K, 60 min, 8×10^{-5} mbar, Linde, purity 99.9999%). To this end, the sample was annealed at 923 K for 10 min and cooled below 300 K, both in O_2 atmosphere (4×10^{-8} mbar, Linde, purity 99.999%). A subsequent heating step to 923 K in UHV was applied to remove residual O_2. The adsorption of CO at 300 K (1×10^{-6} mbar, Westfalen 99.97%) was investigated by IRAS to check the cleanliness of the sample. Traces of carbonyls were removed from the supplied CO via a homebuilt liquid nitrogen trap, combined with a commercial adsorption filter (Pall Gaskleen II). After the stepwise CO adsorption, the sample was either briefly heated to 623 K to remove the adsorbed CO or exposed to a CO atmosphere (> 20 L, 300 K) to saturate the surface.

Deposition of $[C_4C_1Pyr][NTf_2]$. Thin films of the IL (thickness ~ 10 ML) were prepared by evaporation from a home-built Knudsen cell in form of a glass crucible loaded with $[C_4C_1Pyr][NTf_2]$ (Merck KGA, ≥ 98%). The evaporator was pumped via a separate high vacuum line and baked at moderate temperatures for 24 h to aid degassing of the IL prior the experiments. For deposition, the IL was preheated to 400 K and the shutter blocking the beam path was removed to start of the experiment.

Temperature-programmed IRAS (TP-IRAS). IR spectra were acquired while heating the samples with a linear heating ramp (1 spectrum/min, heating rate of 2 K/min, p-polarized light). The recorded data were adjusted for the dampening of IR signals with increasing temperature using the procedure described by Xu et al. [33]. The spectra were referred to the annealed sample at the end of the temperature ramp (700 K). Additionally, differential IR spectra were recorded by dividing each spectrum *i* by its predecessor *i-1*.

Polarization-modulated IRAS (PM-IRAS). The polarization modulation-infrared reflection absorption (PM-IRA) spectra were recorded with a FTIR spectrometer (Bruker Vertex 80v) with a KBr beam splitter and a liquid N_2-cooled HgCdTe detector. In the optical path prior to the sample, a polarizer and a photoelastic modulator (2f = 100 kHz, Hinds) were installed. The reflected IR beam was collected by a BaF_2 focusing lens and directed to the detector. The modulated signal from the detector was processed by a lock-in amplifier (Stanford Research Systems).

Remote-controlled mass flow and pressure controllers (both from Bronkhorst) allowed precise control of the pressure and gas flow within the PM-IRAS reactor chamber. To remove remaining traces of metal carbonyls from the CO (Linde, > 99.997%), the gas was fed through a thermal carbonyl trap (Leiden Probe Microscopy) and further purified by an adsorptive gas purifier (Gaskleen II Purifier, Pall Corporation).

The preparation of the Pd(111) single crystal and deposition of the IL thin films is described above. For the PM-IRAS experiments, the UHV-prepared samples were transferred through ambient conditions to the PM-IRAS reactor chamber. Subsequently, the reactor chamber was evacuated for 2 h to remove traces of water in the system. The thin IL layer protected the single crystal surface from contamination during the transfer from the UHV chamber to the PM-IRAS reactor in air. To obtain an IL-free Pd surface for the reference experiments, we proceeded as follows. The sample was heated in 20 vol% O_2 in Ar at 1 bar and a flow of 10 mL_N/min to 673 K (ΔT = 10 K/min). At this temperature, the reactor chamber was evacuated and flushed with 20 vol% H_2 in Ar at 10 mL_N/min for 6 min. Thereafter, the reactor chamber was evacuated, and heating was stopped at a pressure of ~ 1 mbar. During the cooling process, CO was introduced to the chamber (10 mL_N/min, 1 bar) starting at 473 K. The procedure was applied twice. After the second cleaning procedure, the sample was heated to 523 K (10 K/min) in CO (10 mL_N/min, 1 bar). Finally, the sample was cooled to RT in 1 bar CO.

Following the cleaning procedure, an identical experimental procedure was applied to the pristine Pd(111) and the $[C_4C_1Pyr][NTf_2]$/Pd(111) sample. Both samples were exposed to CO at gradually increasing pressures up to 1 bar until the spectra showed no further changes. Afterwards, a heating ramp was performed in 1 bar CO (10 mL_N/min) to 673 K (ΔT = 2 K/min). During the experiment, PM-IRA spectra were recorded with a resolution of 2 cm^{-1} and an acquisition time of 2 min. The acquired spectra were normalized to account for changes in reflectivity upon heating,[33] the superimposed Bessel function was subtracted, and the spectra were baseline-corrected. To improve the

signal-to-noise ratio, three consecutive PM-IRA spectra were averaged.

Molecular dynamics (MD). Fully atomistic MD simulations were performed with the Large-scale Atomic/Molecular Massively Parallel Simulator (LAMMPS) with the code version from 29th October 2020 and the additional GPU package for acceleration [34]. The integration step for all simulations was set to 1.0 fs. To impose constant temperature, all systems were coupled to the Berendsen thermostat with a relaxation constant of 0.5 ps [34]. The atomic interactions were described by molecular mechanics potentials using a cut-off delimiter of 12 Å along with the shifted-force implementation to avoid force fluctuations near the cut-off distance. Long-range electrostatics were considered by the damped Coulomb approach [35] using a damping parameter of 0.55 $Å^{-1}$ which is determined by a damping parameter study (see Supporting Information, SI) to mimic Ewald summation [36].

The partial charges were determined using Gaussian 09, revision D.01 code, via the "restricted electrostatic potential" (RESP) method at the HF/6-31G* level and refined by the antechamber tool from the Amber20 package. A full list of all atom charges is provided in the SI. The General AMBER Force Field (GAFF) 2.11 suite, as released with the Amber20 package [37] was used for describing the IL and its interactions with CO and the metal substrate. In turn, for the CO-Pd interactions we used the specific model reported in ref. [38] which was demonstrated to show near quantum chemical accuracy. The CO-CO interactions were described by a three-sided model as adopted from [39], whereas the Pd-Pd interactions were taken from [40], respectively.

The (111) Pd surface is modeled by a 2D periodic slab of about 20 Å thickness arranged normal to the z direction. The dimensions of the simulation box in x and y direction (surface coordinates) were chosen as 99×100 $Å^2$ whereas an extension of 110 Å is applied along the z direction. Normal to the Pd surface, our model thus features a 90 Å sized gas phase or vacuum. The latter is terminated by a repulsive wall.

To this basic system setup, we then added IL molecules in a charge-balanced manner. Different degrees of coverage were considered, starting with submonolayers of IL, full monolayers (MLs), and finally multilayers/thin films. Our submonolayer model was chosen as a coverage of 18 IL ion pairs (IPs) per 99 nm^2 surface area. In turn, our largest multilayer model comprises 450 IPs per 99 nm^2. Between these limits, differently dense IL layers were generated on the Pd slab at density intervals of 18 IPs per 99 nm^2 leading to 25 different systems. Each of these systems was relaxed from 95 ns scale MD runs to ensure convergence of total energy and structural data, before final sampling from additional 5 ns runs (see illustration in Fig. 1a).

The interplay with CO was explored from two different types of simulation models. For the models describing co-adsoprtion, a CO adsorbate layer on Pd (111) was prepared with a surface coverage of $\theta_{CO} = 50\%$ (attaching 756 explicit CO molecules to the surface slab model). For this, each CO molecule was randomly placed at one of the ideal adsorption sites. Next, IL molecules were added following the procedure described above. Thus, another 25 co-adsorption systems are obtained which can be compared with the 25 systems describing the pure IL layers on the Pd surface. Further, we explored CO penetration via pure IL layers by adding a gas atmosphere to the Pd-IL models. To boost IL permeation, the number of CO molecules is chosen as 1.5 times as would be necessary for 50% coverage of the Pd surface beneath the IL layer. For the thickest IL layer model exhibiting no CO permeation, this approach leads to a pressure of 100 atm.

3 RESULTS AND DISCUSSION

3.1 Effect of Preadsorbed CO on the $[C_4C_1Pyr][NTf_2]$/Pd(111) interface - MD Simulations

Detailed insights into both the wetting layer and the overlying multilayers in the IL/Pd system were derived from MD simulations. In particular, we study CO-induced changes of the structural orientation of IL molecules on the Pd surface. For this purpose, it is useful to use a classification in terms of the predominant adsorption motifs, which we perform in analogy to previous studies [27]. We label the adsorption motifs of $[NTf_2]^-$ with two indices "*i*-*j*", indicating the number (0 to 2) of Pd-O interactions of the oxygen atoms of each of the two SO_2 moieties, respectively. The motifs for the $[C_4C_1Pyr]^+$ cation are labelled according to the chains/parts of the molecule pointing away from the Pd slab. Illustrations of the adsorption motifs of are provided in Fig. 1b.

We first examined $[C_4C_1Pyr][NTf_2]$ film formation of Pd(111) as a function of surface coverage. Starting with a rather small number of IPs (18 per 99 nm^2), we added further IL pairs in a step-wise manner and contrasted the resulting arrangements in terms of predominant adsorption motifs during the evolution from sub-monolayers to multilayers. Figure 1 depicts the MD-derived conformer analysis of $[NTf_2]^-$ (Fig. 1c) and $[C_4C_1Pyr]^+$ (Fig. 1d) on the pristine Pd(111) surface. At low coverages (18 to 90 IPs), the "1–1" motif is most dominant for the anion. This "flat" arrangement however appears as quite space-demanding and upon adding further IPs we observe increasing occurrence of the less space-demanding adsorption motifs "2–2" and "2 – 1". This indicates that the $[NTf_2]^-$ anions reorient to form a more densely packed wetting layer and marks the point at which a

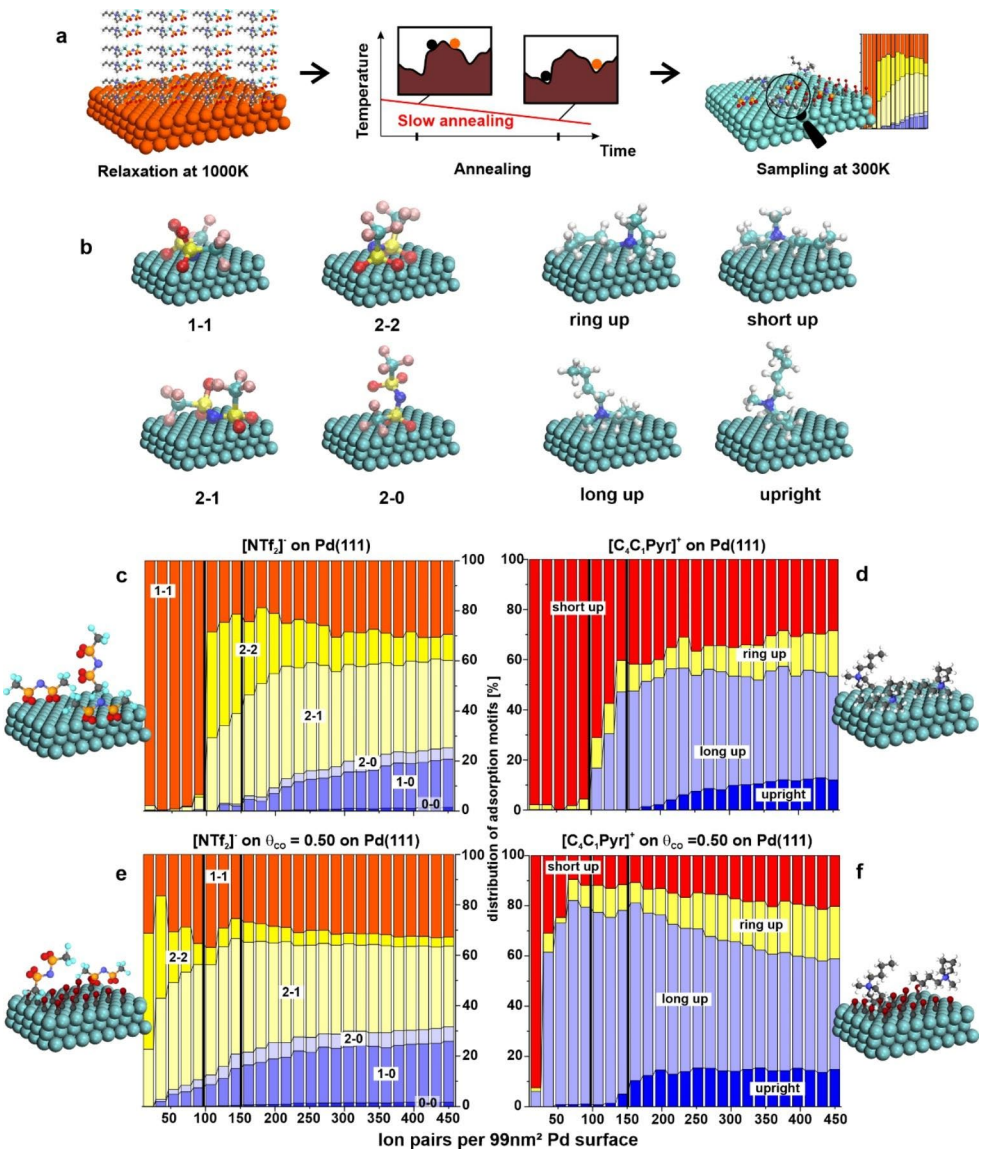

Fig. 1 Top: (a) Illustration of the MD simulation process: initialization by placing molecules in generic pattern - relaxation at 1000 K and annealing to 300 K - sampling and analysis of adsorption motifs; (b) selected adsorption geometries for $[NTf_2]^-$ (left) and $[C_4C_1Pyr]^+$ (right). Bottom: Conformational analysis of (c) $[NTf_2]^-$ on Pd(111), (d) $[C_4C_1Pyr]^+$ on Pd(111), (e) $[NTf_2]^-$ co-adsorbed with CO on Pd(111), (f) $[C_4C_1Pyr]^+$ co-adsorbed with CO on Pd(111) is shown as a function of the number of IPs and the distribution of the respective adsorption motifs. Submonolayer, ML, and multilayer regions are separated by vertical lines (black)

complete ML is formed. Accordingly, the full monolayer is identified as 144 IPs per 99 nm². This point of maximum ML densification is reached at ~ 1.5 times the minimum number of IL needed for full coverage of the Pd(111) surface. Models comprising more than 144 IPs showed the formation of extra layers, whilst no significant changes in anion conformation within the contact ML are observed.

For $[C_4C_1Pyr]^+$ interactions with the Pd surface (Fig. 1d), we differentiate between the more space-demanding motifs "ring up" and "short up" and the less space-demanding motifs "long up" and "upright". In the sub-monolayer regime (18 to 90 IPs), $[C_4C_1Pyr]^+$ accumulates as "short up" conformers. After formation of a full wetting layer (90 IPs), $[C_4C_1Pyr]^+$ cations partially reorient to the less space-demanding "long up" motifs. This progresses up to 50% conversion of the "short up" motifs when reaching the full ML density (144 IPs). In the multi-layer systems, the $[C_4C_1Pyr]^+$ species also adopts the more upright standing adsorption motifs "ring up", "long up" or even "upright".

In summary, we find three distinct coverage regimes in the $[C_4C_1Pyr][NTf_2]$/Pd system which differ in terms of predominant adsorption motifs: submonolayer (< 90 IPs, arranged as space-demanding conformers), densified ML (90–144 IPs, which partly reorganize to less space-demanding conformers), and multilayer (> 144 IPs). We find striking differences between the IL orientation within the layer in direct contact to Pd (referred to as wetting layer) and the IL arrangement in additional layers located further away from the surface. In turn, the structural alignment within the wetting layer remains intact regardless of the number of overlying IL layers.

We then investigated the influence of preadsorbed CO molecules on the nature of $[C_4C_1Pyr][NTf_2]$ submono-/mono-/multilayers. For this, the surface coverage of

θ_{CO} = 50% of a thermodynamically stable CO-saturated Pd (111) surface at RT was implemented to the Pd (111) slab before re-evaluating IL association (see experimental and SI for further details). A direct consequence of this treatment is the packing of IL molecules in favour of less space-demanding adsorption motifs, namely "2–2" and "2 – 1" simultaneous to "1–1" conformers of $[NTf_2]^-$ (Fig. 1e). Similarly, the less space-demanding "short up" and "long up" motifs are observed for $[C_4C_1Pyr]^+$ in the CO pre-treated submonolayer systems (Fig. 1f). These findings indicate that the IL molecules intercalate the preadsorbed CO layer by adopting a space-saving conformation. In turn, this causes the compression of the CO adsorbate layer. This carries on during ML formation (90 to 144 IPs), and the maximum degree of compression of the CO-IL adsorbate layer is reached at 144 IPs in full analogy to the CO-free systems described above. Indeed, we find IL association to the CO pre-treated surface follows similar adsorption motifs as observed for the full ML of IL adsorbed to the pristine Pd surface. Ions in the IL multilayer are loosely bound to the underlying wetting layer and the IL-IL interaction is dominant (see Figure S1 and gif S1). This leads to 3D island growth of the IL multilayer on top of the dense CO/IL co-adsorbate layer. Interestingly, the IL shows the opposite behaviour in case of dominant Pd-IL interaction, i.e., in case of a pure Pd surface or if only a small amount of IPs are added up to maximum compression of the CO adsorbate layer. Here the IL shows layer-by-layer growth.

3.2 Effect of Preadsorbed CO on $[C_4C_1Pyr][NTf_2]$/Pd(111) interface - IRAS Studies

Next, we exploit the insights from the MD simulations to interpret IRAS experiment on the $[C_4C_1Pyr][NTf_2]$/CO/Pd(111) system. As a basis for the assignment of the IR bands, we briefly revisit the multilayer spectrum of $[C_4C_1Pyr][NTf_2]$ in UHV (Fig. 2, multilayer film deposited by PVD on Pd(111)). The peak assignment in Table 1 is based on DFT data, attenuated total reflection (ATR) spectra [27, 31] and previous IRAS studies on other metal supports [26–28, 31]. Note that for IRAS measurements, the so-called metal-surface selection rule (MSSR) applies; only dipole moments of the adsorbates along the surface normal are visible [41].

In general, the experimental IRA spectra agree well with the ATR spectra proving deposition of the IL film without any indication for decomposition.

We prepared $[C_4C_1Pyr][NTf_2]$ films on CO-precovered Pd(111) by exposing Pd(111) to CO until saturation and subsequent deposition of $[C_4C_1Pyr][NTf_2]$ by PVD (Fig. 3a). Subsequently, a linear heating ramp (2 K min^{-1}) was applied while continuously recording IR spectra (acquisition time 45 s). The IR data is also visualized as differential

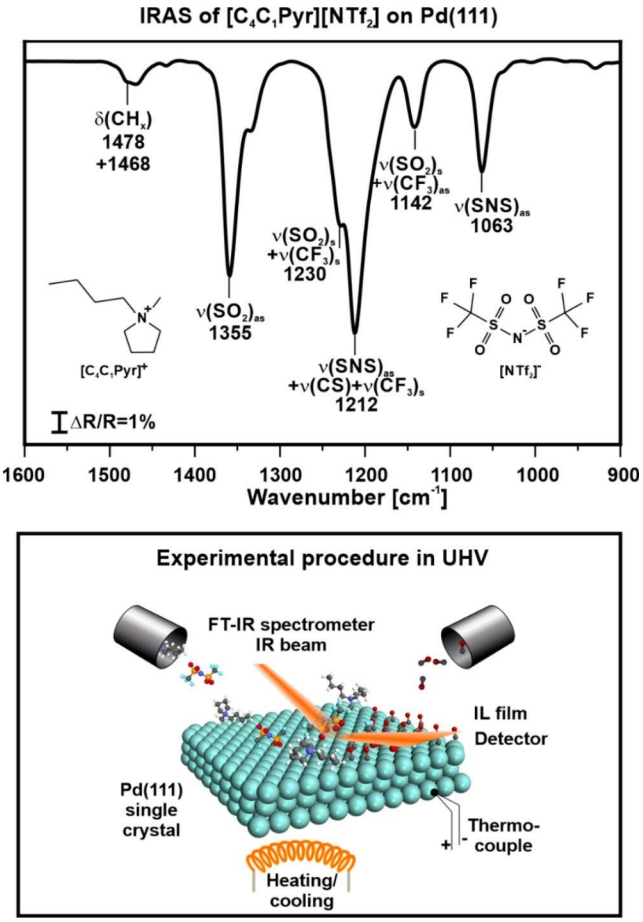

Fig. 2 IRA spectra of $[C_4C_1Pyr][NTf_2]$ multilayer, prepared by PVD onto Pd(111), together with a schematic illustration of the in situ UHV IRAS setup

Table 1 IL peak assignment based on $[C_4C_1Pyr][NTf_2]$ multilayer spectrum on Pd(111)

Peak position	Assignment [26–28, 31]
1355 cm^{-1}	$\nu(SO_2)_{as}$
1230 cm^{-1}	$\nu(SO_2)_s+\nu(CF_3)_s$
1212 cm^{-1}	$\nu(SNS)_{as}+\nu(CS)+\nu(CF_3)_s$
1142 cm^{-1}	$\nu(SO_2)_s+\nu(CF_3)_{as}$
1063 cm^{-1}	$\nu(SNS)_{as}+\nu(CF_3)_s+\nu(SO_2)_s$
1468 cm^{-1}	$\nu(CH_x)$

spectra using the predecessing spectrum as a background ($S_{diff} = S_i/S_{i-1}$). These spectra reflect minute changes in the IR spectrum as a function of temperature.

We first consider the changes of the IL bands in Fig. 3b. Note that the differential plots reflect the dynamic changes on the timescale of the experiment (1 min) with positive bands (pointing up) indicating a loss of intensity while negative bands (pointing down) indicate a gain. S-shaped bands indicate a shift in the vibrational frequency. We observe small positive and s-shaped signals at 1358, 1209, 1133, and 1063 cm^{-1} between 300 and 370 K, which increase in

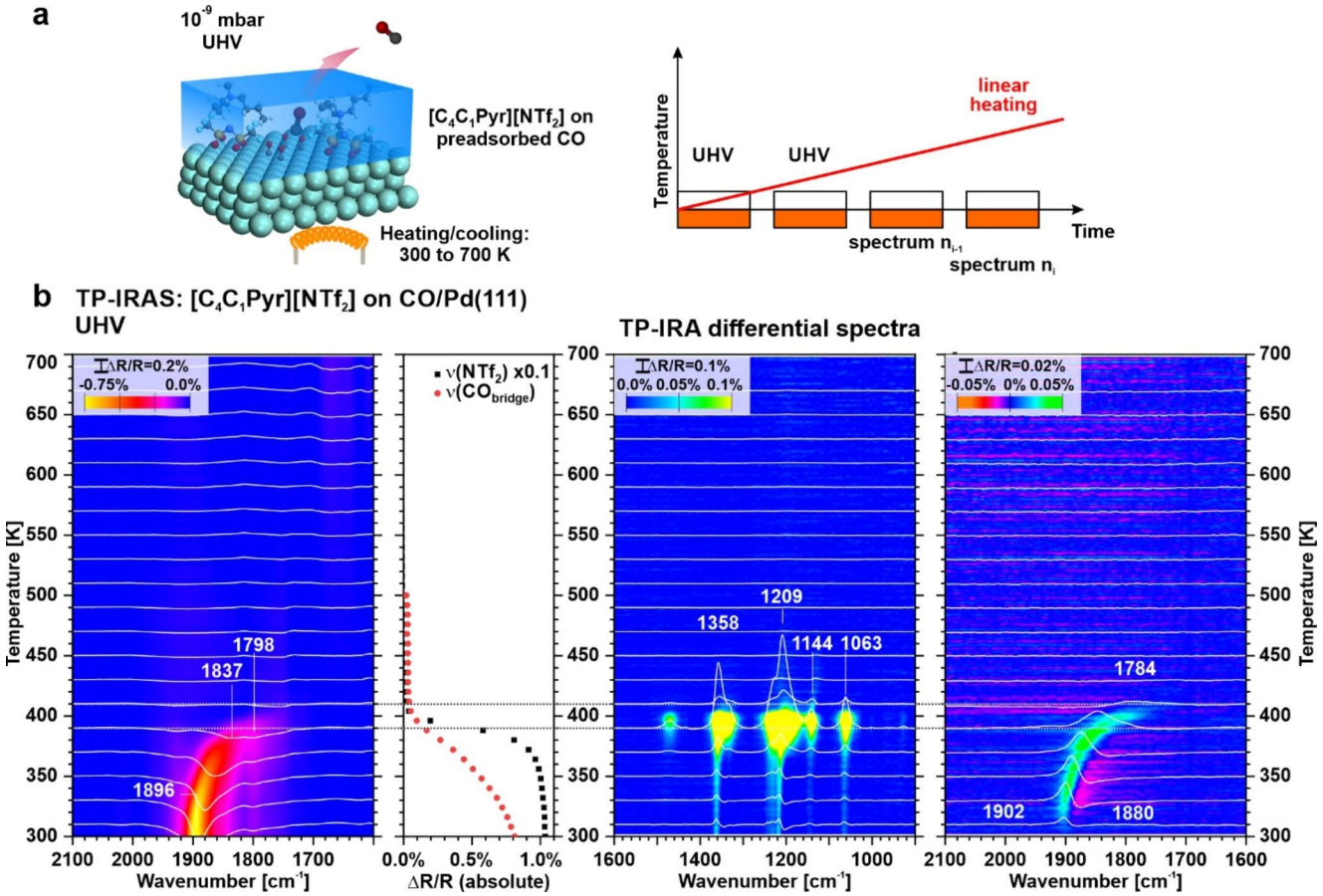

Fig. 3 Time-resolved and temperature-programmed IRAS experiments showing the dynamic adsorption/desorption processes on CO pre-saturated and IL-precoated Pd(111). (a) Experimental setup; (b) from left to right: IR spectra in the CO region acquired during heating (under UHV); integrated intensities of the CO_{br} bands and $[NTf_2]^-$ bands; differential IRA spectra (S_{diff}) in the $[NTf_2]^-$ region and CO region

intensity at 380 K and disappear above 400 K. The signals indicate a dewetting transition and subsequent desorption of the multilayer [31]. In contrast, we observe weak peaks characteristic for the IL wetting layer even above 400 K. This observation shows that the IL wetting layer remains intact after desorption of the multilayer. The weak bands on the multilayer at higher temperature demonstrate that desorption and/or decomposition of the remaining IL ML.

In Fig. 3b, we present two sets of spectra for the CO desorption from the CO-saturated and IL-coated Pd(111) sample. In the left panel, the absolute signals are shown. We observe a dominating signal at 1896 cm^{-1}, which decreases in intensity, shifts to 1837 cm^{-1}, and disappears at 390 K. Simultaneously, a broad and weak signal at 1798 cm^{-1} appears, which first increases in intensity and then disappears at 390 K. In the right panel, we display the differential plot. Here, we observe an s-shaped signal around 1900 cm^{-1}, which increases in intensity up to 370 K. Above this temperature, we observe a desorption signal at 1784 cm^{-1}, which disappears above 400 K.

We assign the signal at 1896 cm^{-1} to CO on bridge sites (CO_{br}) that are red-shifted by the co-adsorption of the IL. Similar shifts we observed in previous work and mainly attributed to a Stark shift originating from the interfacial electric field induced by the of the IL co-adsorbates [3]. Thus, the shift demonstrates the formation of a mixed CO/IL layer in agreement with the findings from MD. The shift of the band to lower wavenumbers with increasing temperature is attributed to CO desorption, which results in reduced dipole coupling [41, 42]. Based on the conformational changes observed in MD simulations, we attribute the signal at 1798 cm^{-1} to CO adsorbates on de-occupied Pd sites created by changes in the binding motif of $[NTf_2]^-$ upon dewetting in the multilayer [27]. Furthermore, competitive adsorption of IL and CO species leads to early desorption of CO. Compared to CO adsorbed on pristine Pd(111), the desorption temperature of CO in the presence of the IL is lowered from 470 K to 390 K (see below), which is in line with our previous studies [43].

Our combined insights from MD simulations and IRAS studies show that there are mutual interactions between CO

and IL adsorbates in wetting layer of the model SCILL. Coadsorbed CO induces structural changes in the IL wetting layer and compression effects lead to a substantially lowered CO desorption temperature.

3.3 CO Permeability of $[C_4C_1Pyr][NTf_2]$/Pd(111) - Molecular Dynamics

Next, we focus on the association of CO to IL thin films as a post-processing step. For this, we revisit our MD simulation models of Pd (111) surfaces covered by an IL submonolayer (18 to 72 IPs = 0.2 to 0.8 ML), MLs (90 to 144 IPs = 1.0 to 1.5 ML), and multilayer films (162 to 450 IPs = 1.8 to 5.0 ML). To each of these models, a CO gas atmosphere at 300 K was added and subjected to 200 ns scale MD runs. Relaxation was monitored in terms of the z-density profiles. Despite the initially 100 bar pressure of the CO gas reservoir, we find only partial relaxation of the Pd-IL-gas interfaces. Only the models with 18 to 72 IPs showed CO permeation between the IL layer in analogy to the CO pretreated systems. For the MD runs featuring a full wetting layer (90 IPs) or even several ML (investigated for up to 450 IPs) we find isolated events of CO association to the Pd surface occurring within time scales of 100 ns and beyond.

To compare the different scenarios in terms of energy, we therefore deleted 2/3 of the CO molecules from the gas atmosphere and, after 5 ns scale relaxation, contrasted the average system energy to that of the corresponding CO-pretreated models. In agreement with our structural analyses, we find roughly equal energy levels for the models comprising up to 54 IPs. In turn, our models featuring more than 144 IPs consistently shows energetic favoring of CO association to Pd by 27.66 kcal/mol (see also supporting figure Fig S2). While we cannot reach the thermodynamic equilibrium within the short time scales of our MD runs, we can still analyze fundamental aspects of (yet incomplete) CO penetration from a more qualitative viewpoint. The local mass density profiles after 200 ns are shown as a function of distance from the surface in Fig. 4. In the MD run featuring the IL submonolayer (highlighted in red), penetrating CO molecules account for two peaks at ~1.5 and 2.75 Å distance to the surface (see Figure S3 and gif S2, S3). For the

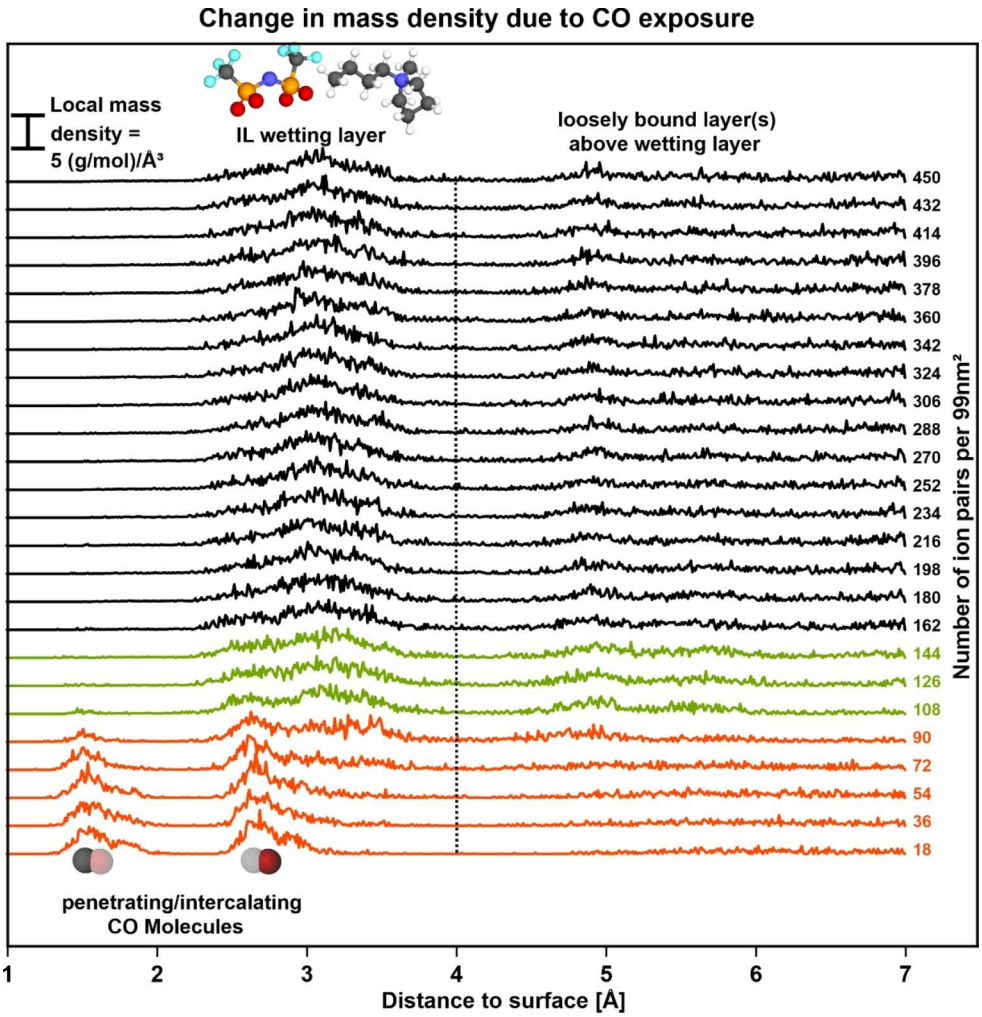

Fig. 4 Analyses of Pd-IL interfaces with a ~ 100 bar CO gas atmosphere. The local mass density profiles as functions of the distance from the surface and the number of IPs are sampled for snapshots taken after 200 ns MD runs. Subject to the number of IP associated to the metal surface, interface relaxation is incomplete. The wetting layer is separated from the overlying molecules by the vertical line. Penetration by CO is clearly visible in submonolayer (red curves), whereas it decreases in the ML (green curves) and is no longer visible in the multilayer (black curves)

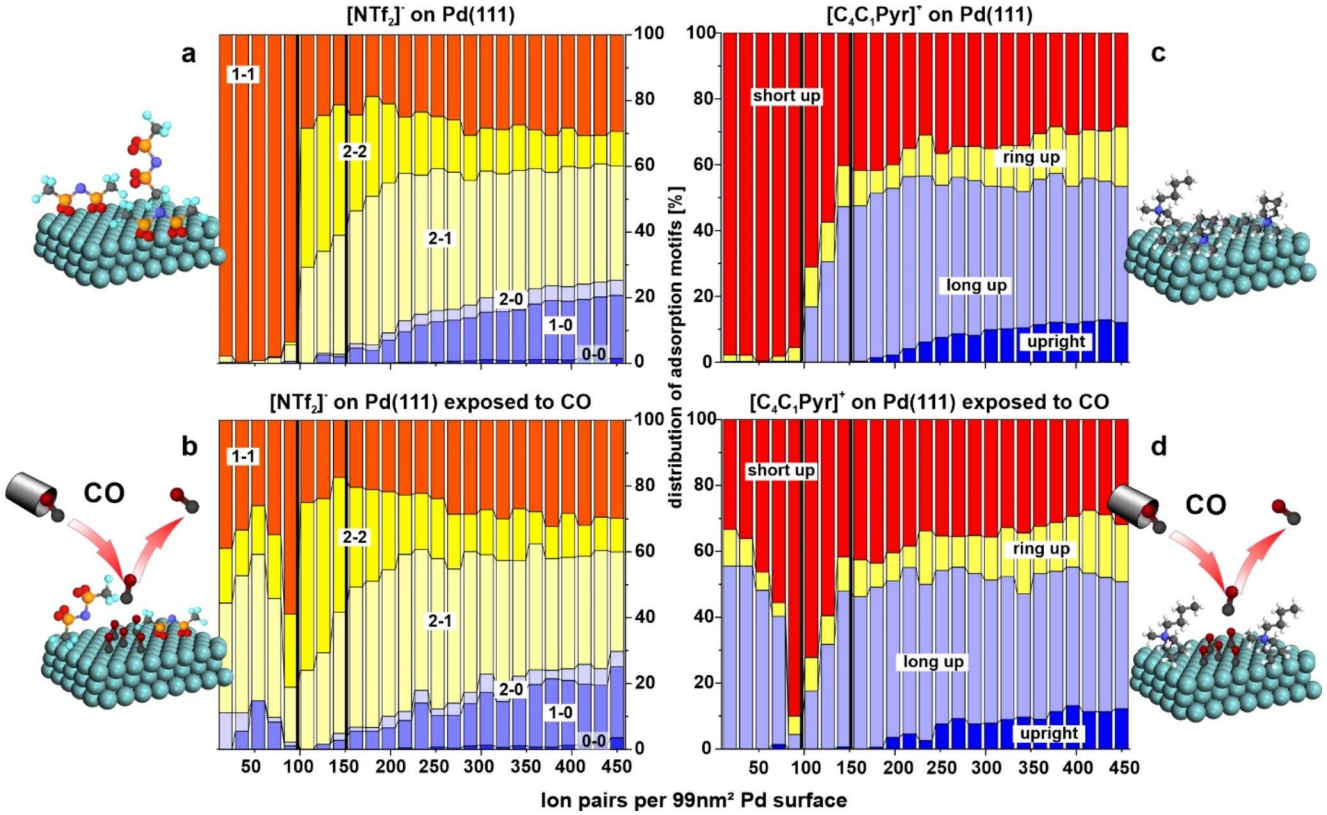

Fig. 5 Conformational analysis of (a) $[NTf_2]^-$ on Pd(111), (b) $[NTf_2]^-$ on Pd(111) exposed to CO, (c) $[C_4C_1Pyr]^+$ on Pd(111), (d) $[C_4C_1Pyr]^+$ on Pd(111) exposed to CO – as obtained after 200 ns scale relaxation. The distribution of the respective adsorption motifs is shown as a function of the number of IPs. Submonolayer, ML, and multilayer regions are separated by vertical lines (black)

interface models featuring larger numbers of IPs, the occurrence of direct CO-Pd contacts after 200 ns relaxation runs is significantly lower (in some cases even zero) (see gif S4). Discrimination of the mass density profiles in terms of CO, anion and cation species are provided in the supporting figure (Fig S4 to S7).

In Fig. 5, we show the analysis of the adsorption motifs at all IL coverages with and without overlying CO atmosphere. Due to the slow permeation of the IL layer by CO, we caution that only the data for 54 IPs or less may be considered as safely converged. In turn, the models featuring CO gas atmospheres in contact to interfaces of more than 72 IPs refer to intermediate (200 ns) snapshots.

For better comparison, the IL conformations on pure Pd(111) are shown in Fig. 5a, c. Due to the slow adsorption kinetics of CO, it is difficult to achieve a fully equilibrated system on this space and time scale of the simulation. However, an equivalent, fully equilibrated system could be obtained by annealing an CO adsorbate layer ($\theta_{CO} = 50\%$) with the same number of IPs (compare Fig. 1). Compared to the CO-free system, we observe dramatic changes in the IL conformation, in particular in the submonolayer regime. In particular, the less space-demanding adsorption motifs are already dominant at very low IL coverage. This observation demonstrates that IL submonolayers (< 90 IP per 99 nm²) are heavily affected by CO intercalation in terms of the adsorption motifs in the wetting layer. These conformational changes are similar to the effect of densification of the $[C_4C_1Pyr][NTf_2]$ film at coverages of 90–144 IP per 99 nm² in the absence of CO (compare Fig. 5a, c). In particular, we observe the appearance of energetically less favorable conformers which are then displaced even more easily by further CO molecules. The CO molecules cause structural changes of the IL wetting layer but do not induce IL desorption (see Figure S3). Note that in the submonolayer regime, the structural changes in the IL are independent of the sequence of adsorption. The IL is mobile enough to allow for the formation of a compressed co-adsorbate layer via formation of less-space demanding conformers in the wetting layer.

Upon densification of the IL film (> 90 IPs), the IL ions adopt less space-demanding motifs both in the absence and presence of CO. Furthermore, we find that the compressed IL ML as well as the IL multilayer (> 144 IPs per 99 nm²) is not permeable for CO molecules.

3.4 CO Permeability of $[C_4C_1Pyr][NTf_2]$/Pd(111) – IRAS Studies

Next, we studied the permeability of IL films (approx. 10 ML) for CO experimentally by IRAS (see Fig. 6a). We heated the IL films (2 K min^{-1}) and simultaneously applied CO pulses (10^{-5} mbar CO for 45 s, UHV for 75 s). IR spectra were recorded during each interval. We obtained three sets of spectra, namely (i) one set recorded under CO pressure (S_{CO}), (ii) one set recorded under UHV conditions (S_{UHV}), and (iii) one set of differential spectra ($S_{diff} = S_{CO} / S_{UHV}$). The differential spectra reflect the dynamic adsorption and desorption processes induced by pressure modulation (timescale 60 s). Further information refer to the experimental section and our previous work [44].

For comparison, we present three sets of data for CO adsorption on clean Pd(111) in Fig. 6b. Spectra recorded in CO atmosphere (S_{CO}, left panel) show a signal at 1936 cm^{-1} at 300 K. The signal shifts to lower wavenumbers and decreases in intensity, until it disappears at 1814 cm^{-1} above 550 K. In agreement with the literature, we assign the signal at 1936 cm^{-1} to mixture of CO_{br} and CO on three-fold hollow sites (CO_h). With increasing temperature, the band shifts towards to the singleton frequency of isolated CO_h, indicating the desorption of the more weakly bound CO_{br} adsorbates [45]. The results are in good agreement with

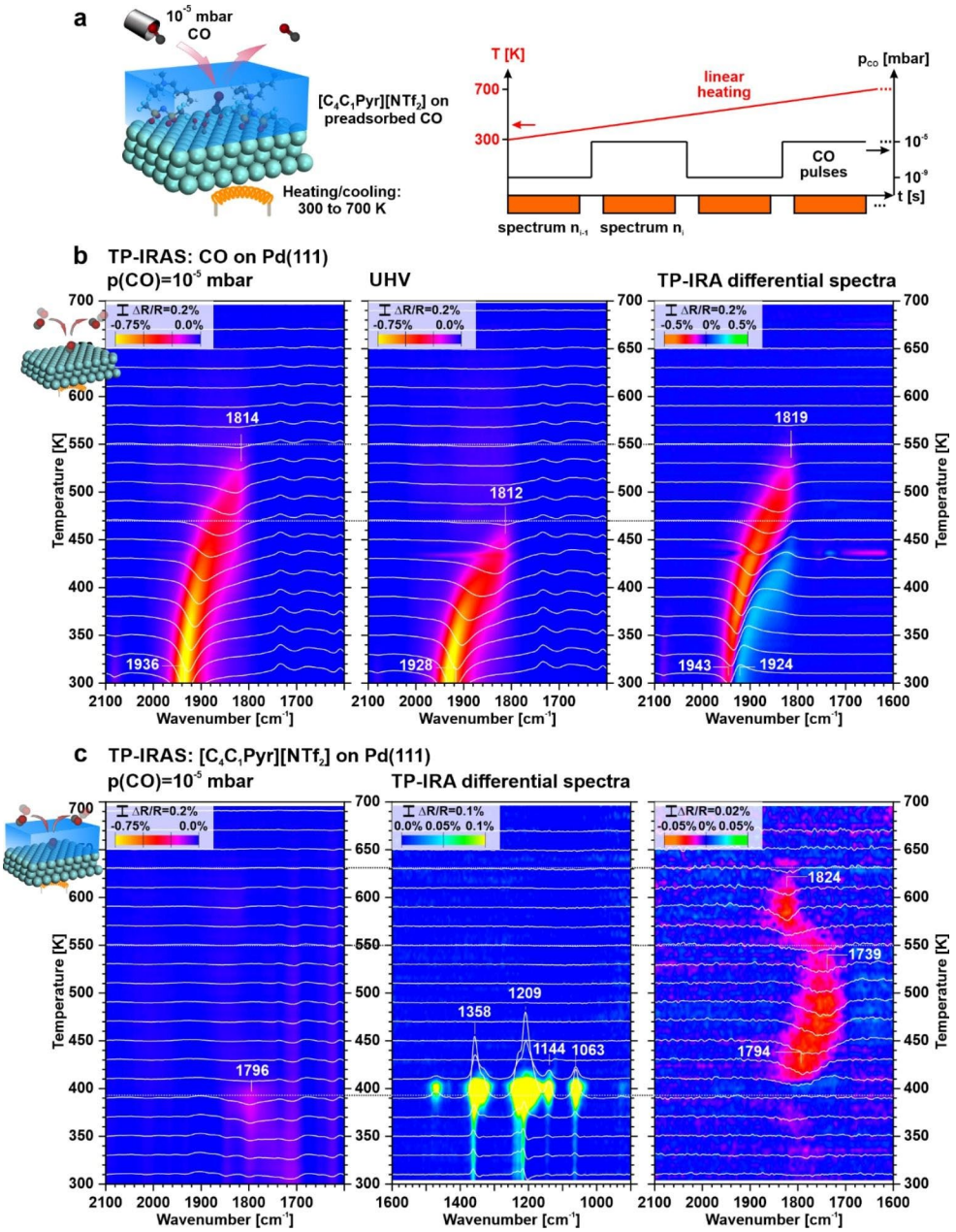

Fig. 6 Time-resolved and temperature-programmed IRAS experiments showing the dynamic ad/desorption processes on clean and IL-coated Pd(111). (a) Experimental procedure; (b) IR spectra acquired during CO pulses and heating of clean Pd(111); (c) IR spectra acquired during CO pulses and heating of IL-coated Pd(111)

temperature-programmed desorption (TPD) experiments, but the characteristic changes occur at higher temperatures due to the background pressure of CO [46, 47]. The spectra recorded in UHV (S_{UHV}, Fig. 6b,) display a similar trend, but desorption occurs at 80 K lower temperature. This data resembles the TPD data if we take into account the lower heating rate of 2 K/min [46, 47].

In the differential plot (s_{diff}, right panel) in the region from 300 to 470 K, the s-shaped band originates from the shift of the CO stretching band when the coverage changes as a result of the CO pressure. It is, therefore, a signature of dynamic ad/desorption of CO_{br} [42, 48]. The signal observed between 470 and 550 K results from dynamic ad/desorption of CO_h. Above 550 K, no changes are observed, since the binding energy of CO is too low for adsorption at these temperatures.

In Fig. 6c, we display the results after repeating the same experimental procedure for a sample loaded with an IL multilayer (10 ML) on Pd(111). The recorded data are plotted as absolute (S_{CO}, left panel) and differential spectra (S_{diff}, IL bands in center panel, CO bands in right panel). Below 390 K, the appearance of s-shaped IL bands indicates band shifts due to changing molecular interactions within the multilayer. An IL film can exhibit different growth morphologies, such as layer-by-layer growth or 3D islands on a wetting layer [49]. Note, however, that for all IL/metal systems investigated, the first IL ML in contact with the metal surface was found to be a closed wetting layer [50, 51]. The behavior in the temperature-programmed experiments indicates migration of the IL and partial, gradual dewetting in the multilayer (droplet formation) on top of an intact ML film. At 390 K, we observe pronounced bands, which indicate the desorption of the IL multilayer at this temperature.

Up to 390 K, the differential CO spectra do not reveal any bands, while the static CO spectra indicate a band at 1796 cm^{-1} upon heating, which steadily increases in intensity. At 390 K, we observe the loss of the CO band (left panel), which coincides with desorption of the IL. Immediately afterwards, a band at 1794 cm^{-1} appears in the differential CO spectra (right panel). Until 550 K, it gradually red-shifts by 55 cm^{-1} to 1739 cm^{-1} while decreasing slightly in intensity. Above 550 K, the signal at 1739 cm^{-1} disappears and a sharper signal at 1824 cm^{-1} appears, which is lost at 630 K.

We assign the signal at 1796 cm^{-1} observed in the absolute spectra to CO_h co-adsorbed with the IL. The static CO bands indicate an increasing amount of CO which permeates the IL and adsorbs to the Pd surface. In accordance with our MD simulations, we find that CO permeation is not possible for the intact IL multilayer: only upon heating, static CO adsorption occurs through the partially dewetted IL multilayer film. Here, the changing adsorption motif of the anion allows for increased CO adsorption in a less dense IL film [27].

The process, however, is not quick enough to be visible in the differential plots. The amount of CO continuously increases with increasing dewetting. As soon as the IL multilayer has desorbed above 390 K, no static CO adsorption is observed any more. Instead, the differential bands indicate that CO rapidly ad/desorbs dynamically dependent on the pressure. This observation highlights that CO permeation through the remaining IL wetting ML is enhanced after the desorption of the multilayer. The shift of the CO band to lower wavenumbers with increasing temperature is attributed to depopulation of bridging sites. Meanwhile, the more strongly adsorbed CO_h gives rise to the signal at lower frequency. Note that the persistently strong Stark shift of the CO band proves the integrity of the IL wetting ML as the CO species co-adsorb and form a compressed IL/CO layer. Partial dewetting of the IL film and rearrangement of $[NTf_2]^-$ towards the "2–2" motif allows for CO adsorption in between the ions. At 550 K, the CO band position at 1824 cm^{-1} is identical to the one observed for both the pristine Pd(111) at high temperatures (Fig. 6b, right panel) and clean Pd(111) with low coverages of CO [27]. Thus, we assign the feature to CO_h without any Stark shift due to disintegration of the IL wetting ML through desorption or decomposition [52]. Above 630 K, no dynamic CO ad/desorption signal is observed as the steady state coverage in the presence of CO becomes too low (differences to the experiment on clean Pd(111), see Fig. 6b, originate from different scaling on both plots).

In summary, we find that under UHV conditions CO only gradually permeates the IL multilayer film as the latter increasingly dewets in the multilayer region and leaves a wetting ML behind. In the presence of the CO, the IL changes the adsorption motif and the $[NTf_2]^-$ anion adopts a "2 – 0" binding motif. At elevated temperature and after desorption of the IL multilayer, CO dynamically adsorbs and desorbs in the presence of the IL wetting ML. Dynamic CO adsorption and desorption is seen also after breakdown of the IL wetting ML above 550 K and ceases above 630 K. Furthermore, our combined MD and IRAS data demonstrates the ability of the $[NTf_2]^-$ ions to adsorb in different binding motifs and that the adsorption motif changes with the coverage of the CO co-adsorbate.

3.5 CO Permeability of $[C_4C_1Pyr][NTf_2]$/Pd(111) - PM-IRAS Experiments at Ambient Pressure

Finally, we investigate the temperature-dependent CO permeability of the $[C_4C_1PyrNTf_2]$ films on Pd(111) at pressures up to 1 bar. To this end, we apply PM-IRAS measurements. Again, we first performed a reference experiment by heating

of the pristine Pd(111) in CO atmosphere in the absence of the IL (Fig. 7a). We observe a CO bands at ~ 1922 cm^{-1} at 300 K, which decreases in intensity during heating and red-shifts to 1904 cm^{-1} before it vanishes at 560 K.

CO_{br} on Pd(111) at near-ambient pressure of CO and 300 K gives rise to an IR band around 1940 cm^{-1} [53, 54]. The band observed in our experiment is shifted to lower wavenumbers. We attribute the discrepancy to contaminations which reside after the cleaning procedure (for details see Experimental Section). Impurities on the metal surface reduce the coupling between the CO adsorbates and, thus, leads to a peak at lower wavenumbers. Upon heating further, the CO coverage decreases further and the band shifts to 1904 cm^{-1} [55]. The desorption temperature of 560 K is in good agreement with the trend obtained from the experiment in UHV and 10^{-5} mbar CO (470 and 550 K, respectively) [56].

Next, we investigate a Pd(111) sample loaded with an $[C_4C_1Pyr][NTf_2]$ film at different pressures ranging from ~ 1 mbar to 1 bar CO at RT. Figure 7b depicts the corresponding

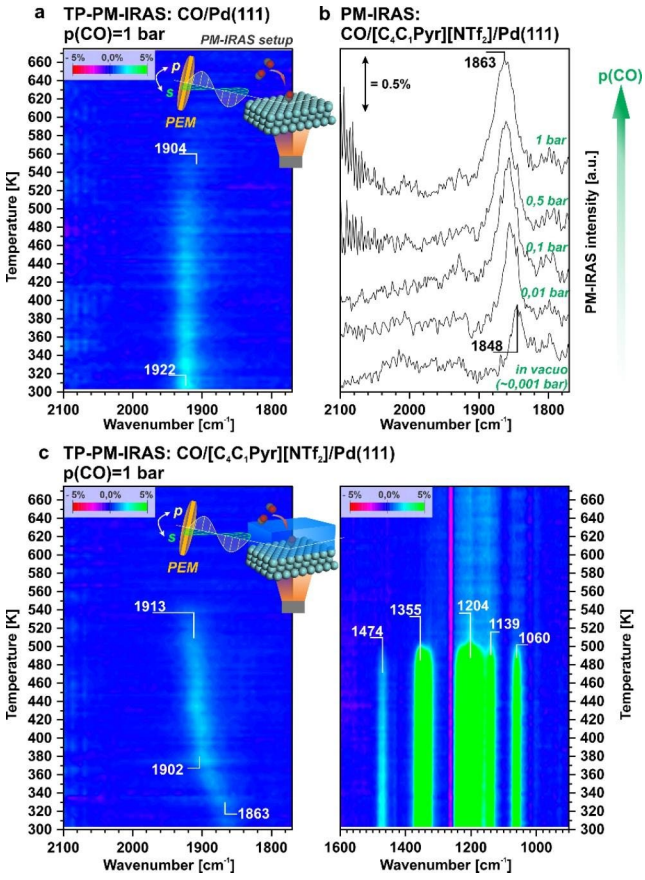

Fig. 7 (a) Color-coded intensity plots of a temperature-programmed PM-IRA experiment for CO/Pd(111), (b) PM-IRA spectra recorded during CO dosing on $[C_4C_1Pyr][NTf_2]$/Pd(111). To improve the signal-to-noise ratio, four consecutive spectra were averaged. (c) Color-coded intensity plots of temperature-programmed PM-IRA spectra of CO/$[C_4C_1Pyr][NTf_2]$/Pd(111)

spectra. In the spectrum recorded in vacuo (~ 1 mbar), a peak at 1848 cm^{-1} is observed due to CO molecules which pre-adsorb to the surface during the UHV preparation. This peak shifts to higher wavenumbers and increases in intensity with a gradual increase of the CO pressure. At 1 bar, the peak is located at 1863 cm^{-1}.

We attribute this peak to CO_{br} co-adsorbed with the IL on Pd(111). In comparison to experiment on pristine Pd(111), we observe a red-shift of 59 cm^{-1} which we attribute to the effect of the co-adsorbed IL [3]. In comparison to the CO adsorption peak observed under UHV conditions (1896 cm^{-1}), the peak at elevated pressure is shifted to lower wavenumbers. This is attributed to the absence of pre-adsorbed CO and possible contaminations, resulting in an overall lower CO surface coverage. We observe a clear pressure dependency of the CO adsorption peak. Note that the most pronounced spectral changes occur at relatively low pressure. We attribute the increase of the CO peak and its shift to higher wavenumbers to adsorption of additional CO after penetration of the IL film [55]. In contrast to the UHV experiments, CO adsorption occurs already at 300 K in the course of the PM-IRAS experiments. We assume that a change of the morphology of the IL film may occur during transfer from UHV to the PM-IRAS setup though ambient conditions. Similar to the trend in the TP-IRAS experiments, partial dewetting of the IL multilayer occurs, presumably due to exposure of the film to moisture during transfer in air [57, 58]. As a result, CO permeates the exposed wetting IL ML already at RT.

Subsequently, we heat the $[C_4C_1Pyr][NTf_2]$/Pd(111) sample to 675 K in 1 bar CO while acquiring PM-IRA spectra. The results are displayed in Fig. 7c. In the IL region, characteristic peaks are visible at 1060 cm^{-1}, 1139 cm^{-1}, 1204 cm^{-1}, 1355 cm^{-1}, and 1474 cm^{-1}. Upon heating, the peaks decrease in intensity until they vanish around 500 K.

The peaks agree with the signals obtained during the UHV experiment (see Table 1 for a detailed assignment). The decreasing intensity of the IL peaks is due to the desorption of the IL multilayer at 500 K. Unfortunately, the IL wetting ML signals are not distinguishable from the noise in the PM-IRA spectra. The fact that desorption occurs at higher temperature compared to the TP-IRAS experiment in UHV (T_{des} = 390 K, see above, and the references [31]) is rationalized by the overall increased pressure in the PM-IRAS setup. Higher background pressure hinders diffusion of desorbed IL molecules away from the sample and enhances re-adsorption of the IL at temperatures above the multilayer desorption temperature in UHV. For an estimation of the adsorption, desorption, and diffusion processes, we refer to the SI.

In the CO region, the peak at 1863 cm^{-1} shifts to 1902 cm^{-1} and, thereafter, with a slower rate to ~ 1913 cm^{-1}.

This is due to two superimposing effects, a reduced Stark shift upon desorption of the IL wetting ML [3] and/or increased coupling between CO adsorbates on Pd(111) [55]. Both effects lead to a shift of the peak to higher wavenumbers. The CO peak intensity, which serves as an indicator for the CO coverage, increases up to 430 K in the presence of an IL multilayer. A further increase of the temperature leads to a loss of CO until the signal vanishes [53].

We conclude that with further heating, the area of partially depleted IL multilayer increases. A change of the IL film morphology towards 3D islands during heating was observed both by Syres et al. [59] and to a lesser extent in the UHV experiment (see above). In consequence, the overall CO permeability of the system increases, which allows for the adsorption of CO through the IL film already below the multilayer desorption temperature. In our experiment, this leads to an increase of the CO coverage and, hence, the increase of the CO band and a shift of the peak position to higher wavenumbers. In comparison to the reference experiment on pristine Pd(111), no shift of the CO peak to lower wavenumbers occurs upon desorption. From that we conclude that at 540 K the IL wetting ML is still present on the surface.

4 Conclusion

In this work, we investigated the interaction of a Pd-based model SCILL system with CO. We combined theoretical insights from MD calculations with experimental data obtained by time-resolved and temperature-programmed IRAS experiments in UHV. In particular, we investigated the mutual interactions of co-adsorbed CO and IL and tested the dynamic ad/desorption as a function of temperature both in UHV by IRAS and at 1 bar CO pressure by PM-IRAS. The main conclusions of the study are summarized in the following:

(1) *Morphology and stability of the IL film*: While being stable at RT, the IL multilayer separates into a strongly adsorbed IL wetting ML and 3D droplets on top upon heating. While the IL multilayers desorbs at 390 K under UHV conditions, the IL wetting ML remains stable up to 550 K.
(2) *CO-induced changes of IL wetting layer*: Pre-adsorbed CO molecules induce conformational changes of the IL, in particular in the wetting layer. Here, the IL adopts less space-demanding conformers in comparison to adsorption of a pristine Pd(111) surface. This makes it possible for CO to co-adsorb in a dense IL wetting layer.
(3) *CO permeability of [C_4C_1Pyr][NTf_2]*: We find that CO permeation does not occur for perfectly closed 2D IL multilayer films. Partial multilayer dewetting, e.g. due to partial desorption/restructuring, however, enables slow accumulation of adsorbed CO from the gas phase through the exposed IL wetting ML. After desorption of the IL multilayer, an IL wetting layer resides, which enables fast and dynamic ad/desorption of CO. The IL wetting layer remains intact upon dynamic CO adsorption and desorption, as demonstrates by both the MD simulations and the IRAS/PM-IRAS experiment. Upon the adsorption of the CO, the IL wetting layer responds to the presence of the co-adsorbate and the ions adopt to less space-demanding adsorption motifs on the surface. At near ambient pressure, CO is able to penetrate the IL layer already at RT. We attribute this effect to the higher background pressure and a more pronounced 3D droplet formation leaving behind the IL wetting layer.

The mutual interactions between the IL wetting layer and probe molecules at the noble metal interface are of fundamental importance for the selectivity control by IL layers in catalytic materials. Combining theory and experiment, we demonstrate the importance of the dynamic nature of the IL wetting layer for the adsorption process in the catalyst surface. We propose that the flexibility of the adsorption motifs of the is a key factor which can be used to control the effect of the IL on the adsorption and reaction behavior.

Supporting information. Supporting Information is available. Investigations of Coulomb interactions for anisotropic Systems; Pd slab model; CO model; CO-Pd interactions; $[NTf_2]^-$ model; $[C_4C_1Pyr]^+$ model, CO incorporation energy per molecule, Discriminated Mass density plots, Calculation of the pressure dependency of the desorption of IL.

Supplementary Information The online version contains supplementary material available at https://doi.org/10.1007/s11244-023-01798-4.

Acknowledgements The authors declare no financial interest. This work was funded by the Deutsche Forschungsgemeinschaft (DFG, German Research Foundation) – Project-ID 431791331 – SFB 1452 (CLINT Catalysis at Liquid Interfaces). The authors acknowledge further support by the DFG via the projects 322419553 and 453560721. The authors gratefully acknowledge the scientific support and HPC resources provided by the Erlangen National High Performance Computing Center (NHR@FAU) of the Friedrich-Alexander-Universität Erlangen-Nürnberg (FAU) under an early-access NHR project. NHR funding is provided by federal and Bavarian state authorities. NHR@FAU hardware is partially funded by the German Research Foundation (DFG) – 440719683. The authors acknowledge additional financial support by the Bavarian Ministry of Economic Affairs, Regional Development and Energy through the Helmholtz Institute Erlangen-Nürnberg for Renewable Energy (HI ERN) (Emission-free and highly emission-reduced rail traffic on non-electrified lines).

Funding Open Access funding enabled and organized by Projekt DEAL.

References

1. Steinrück H-P, Libuda J, Wasserscheid P et al (2011) Surface Science and Model Catalysis with Ionic Liquid-Modified materials. Adv Mater 23:2571–2587. https://doi.org/10.1002/adma.201100211
2. Steinrück H-P, Wasserscheid P (2015) Ionic liquids in Catalysis. Catal Lett 145:380–397. https://doi.org/10.1007/s10562-014-1435-x
3. Bauer T, Mehl S, Brummel O et al (2016) Ligand Effects at Ionic Liquid-Modified Interfaces: Coadsorption of [C2C1Im][OTf] and CO on pd(111). J Phys Chem C 120:4453–4465. https://doi.org/10.1021/acs.jpcc.6b00351
4. Welton T (1999) Room-temperature ionic liquids. Solvents for synthesis and catalysis. Chem Rev 99:2071–2084. https://doi.org/10.1021/cr980032t
5. Wasserscheid P, Keim W (2000) Ionic Liquids?New ?Solutions? for Transition Metal Catalysis. Angew Chemie 39:3772–3789. https://doi.org/10.1002/1521-3773(20001103)39:21<3772::aid-anie3772>3.0.co;2-5
6. Horváth IT, Rábai J (1994) Facile Catalyst separation without Water: Fluorous Biphase Hydroformylation of Olefins. Sci (80-) 266:72–75. https://doi.org/10.1126/science.266.5182.72
7. Wilkes JS (2002) A short history of ionic liquids—from molten salts to neoteric solvents. Green Chem 4:73–80. https://doi.org/10.1039/b110838g
8. Meyer C, Werner S, Haumann M, Wasserscheid P (2015) Chemical Engineering of ionic liquid processes. In: Plechkova NV, Seddon Kenneth R (eds) Ionic liquids completely UnCOILed: critical Expert Overviews. John Wiley & Sons, Inc, Hoboken, NJ, pp 107–144
9. Kernchen U, Etzold B, Korth W, Jess A (2007) Solid Catalyst with Ionic Liquid Layer (SCILL) – A New Concept to Improve Selectivity Illustrated by Hydrogenation of Cyclooctadiene. Chem Eng & Technol 30:985–994. https://doi.org/10.1002/ceat.200700050
10. Cremer T, Killian M, Gottfried JM et al (2008) Physical vapor deposition of [EMIM][Tf_2N]: a New Approach to the modification of Surface Properties with ultrathin Ionic Liquid Films. ChemPhysChem 9:2185–2190. https://doi.org/10.1002/cphc.200800300
11. Barth T, Korth W, Jess A (2016) Selectivity-Enhancing Effect of a SCILL Catalyst in Butadiene Hydrogenation. Chem Eng & Technol 40:395–404. https://doi.org/10.1002/ceat.201600140
12. Meyer C, Hager V, Schwieger W, Wasserscheid P (2012) Enhanced activity and selectivity in n-octane isomerization using a bifunctional SCILL catalyst. J Catal 292:157–165. https://doi.org/10.1016/j.jcat.2012.05.008
13. Bauer T, Hager V, Williams MB et al (2016) Palladium-mediated ethylation of the Imidazolium Cation Monitored in Operando on a Solid Catalyst with Ionic Liquid Layer. ChemCatChem 9:109–113. https://doi.org/10.1002/cctc.201601222
14. Szesni N, Fischer R, Hagemeyer A et al (2013) Catalyst composition for selective hydrogenation with improved characteristics. U.S. Patent WO2013057244A1
15. Arras J, Steffan M, Shayeghi Y, Claus P (2008) The promoting effect of a dicyanamide based ionic liquid in the selective hydrogenation of citral. Chem Commun 4058. https://doi.org/10.1039/b810291k
16. Arras J, Steffan M, Shayeghi Y et al (2009) Regioselective catalytic hydrogenation of citral with ionic liquids as reaction modifiers. Green Chem 11:716. https://doi.org/10.1039/b822992a
17. Arras J, Paki E, Roth C et al (2010) How a supported metal is influenced by an ionic liquid: In-Depth characterization of SCILL-Type Palladium catalysts and their hydrogen adsorption. J Phys Chem C 114:10520–10526. https://doi.org/10.1021/jp1016196
18. Maier F, Cremer T, Kolbeck C et al (2010) Insights into the surface composition and enrichment effects of ionic liquids and ionic liquid mixtures. Phys Chem Chem Phys 12:1905. https://doi.org/10.1039/b920804f
19. Steinrück H-P (2010) Surface science goes liquid ! Surf Sci 604:481–484. https://doi.org/10.1016/j.susc.2009.12.033
20. Wasserscheid P (2006) Volatile times for ionic liquids. Nature 439:797–797. https://doi.org/10.1038/439797a
21. Leal JP, Esperança JMSS, Minas da Piedade ME et al (2007) The Nature of Ionic Liquids in the gas phase. J Phys Chem A 111:6176–6182. https://doi.org/10.1021/jp073006k
22. Armstrong JP, Hurst C, Jones RG et al (2007) Vapourisation of ionic liquids. Phys Chem Chem Phys 9:982. https://doi.org/10.1039/b615137j
23. Lovelock KRJ, Villar-Garcia IJ, Maier F et al (2010) Photoelectron Spectroscopy of Ionic Liquid-Based interfaces. Chem Rev 110:5158–5190. https://doi.org/10.1021/cr100114t
24. Cremer T, Wibmer L, Calderón SK et al (2012) Interfaces of ionic liquids and transition metal surfaces—adsorption, growth, and thermal reactions of ultrathin [C1C1Im][Tf2N] films on metallic and oxidised ni(111) surfaces. Phys Chem Chem Phys 14:5153. https://doi.org/10.1039/c2cp40278e
25. Xu T, Wähler T, Vecchietti J et al (2017) Interaction of Ester-Functionalized Ionic Liquids with Atomically-Defined Cobalt Oxides Surfaces: Adsorption, reaction and Thermal Stability. ChemPhysChem 18:3443–3453. https://doi.org/10.1002/cphc.201700843
26. Sobota M, Nikiforidis I, Hieringer W et al (2010) Toward ionic-liquid-based Model Catalysis: growth, orientation, conformation, and Interaction mechanism of the [Tf 2 N] – anion in [BMIM][Tf 2 N] Thin Films on a well-ordered Alumina Surface. Langmuir 26:7199–7207. https://doi.org/10.1021/la904319h
27. Schuschke C, Fromm L, Träg J et al (2021) A Molecular View of the Ionic Liquid Catalyst Interface of SCILLs: Coverage-Dependent Adsorption Motifs of [C4C1Pyr][NTf2] on pd single crystals and nanoparticles. J Phys Chem C 125:13264–13272. https://doi.org/10.1021/acs.jpcc.1c02131
28. Sobota M, Happel M, Amende M et al (2011) Ligand Effects in SCILL Model Systems: site-specific interactions with pt and pd nanoparticles. Adv Mater 23:2617–2621. https://doi.org/10.1002/adma.201004064
29. Zhang G-R, Munoz M, Etzold BJM (2015) Boosting Performance of Low Temperature Fuel Cell Catalysts by Subtle Ionic Liquid Modification. ACS Appl Mater & Interfaces 7:3562–3570. https://doi.org/10.1021/am5074003
30. Zhang G, Munoz M, Etzold BJM (2016) Accelerating oxygen-reduction catalysts through preventing poisoning with non-reactive species by using Hydrophobic Ionic Liquids. Angew Chemie Int Ed 55:2257–2261
31. Schuschke C, Hohner C, Stumm C et al (2019) Dynamic CO adsorption and desorption through the ionic liquid layer of a Pt

Model Solid Catalyst with Ionic Liquid Layers. J Phys Chem C 123:31057–31072. https://doi.org/10.1021/acs.jpcc.9b09128
32. Schuschke C, Hohner C, Jevric M et al (2019) Solar energy storage at an atomically defined organic-oxide hybrid interface. Nat Commun 10. https://doi.org/10.1038/s41467-019-10263-4
33. Xu T, Schwarz M, Werner K et al (2016) The surface structure matters: thermal stability of phthalic acid anchored to atomically-defined cobalt oxide films. Phys Chem Chem Phys 18:10419–10427. https://doi.org/10.1039/c6cp00296j
34. Thompson AP, Aktulga HM, Berger R et al (2022) LAMMPS - a flexible simulation tool for particle-based materials modeling at the atomic, meso, and continuum scales. Comput Phys Commun 271. https://doi.org/10.1016/J.CPC.2021.108171
35. Zahn D, Schilling B, Kast SM (2002) Enhancement of the Wolf Damped Coulomb potential: static, dynamic, and Dielectric Properties of Liquid Water from Molecular Simulation. J Phys Chem B 106:10725–10732. https://doi.org/10.1021/JP025949H
36. Fennell CJ, Gezelter JD (2006) Is the Ewald summation still necessary? Pairwise alternatives to the accepted standard for long-range electrostatics. J Chem Phys 124. https://doi.org/10.1063/1.2206581
37. Case DA, Aktulga HM, Belfon K et al (2022) Amber22
38. Michalka JR, Gezelter JD (2015) Island formation on Pt/Pd(557) surface alloys in the presence of adsorbed CO: a molecular dynamics study. J Phys Chem C 119:14239–14247. https://doi.org/10.1021/ACS.JPCC.5B03586/SUPPL_FILE/JP5B03586_SI_001.PDF
39. Martín-Calvo A, Lahoz-Martín FD, Calero S (2012) Understanding carbon monoxide capture using metal-organic frameworks. J Phys Chem C 116:6655–6663. https://doi.org/10.1021/JP211563E/SUPPL_FILE/JP211563E_SI_001.PDF
40. Heinz H, Vaia RA, Farmer BL, Naik RR (2008) Accurate Simulation of Surfaces and Interfaces of Face-Centered cubic Metals using 12 – 6 and 9 – 6 Lennard-Jones potentials. J Phys Chem C 112:17281–17290. https://doi.org/10.1021/JP801931D
41. Hoffmann FM (1983) Infrared reflection-absorption spectroscopy of Adsorbed Molecules. Surf Sci Rep 3:107109–107192
42. Hollins P (1992) The influence of surface defects on the infrared spectra of adsorbed species. Surf Sci Rep 16:51–94. https://doi.org/10.1016/0167-5729(92)90008-y
43. Eschenbacher R, Schuschke C, Bühlmeyer H et al (2021) Interaction between Ionic Liquids and a pt(111) surface probed by Coadsorbed CO as a test molecule. J Phys Chem Lett 12:10079–10085. https://doi.org/10.1021/acs.jpclett.1c02983
44. Blaumeiser D, Schuschke C, Fromm L et al (2021) CO Permeability and Wetting Behavior of Ionic Liquids on Pt(111): an IRAS and PM-IRAS study from Ultrahigh Vacuum to ambient pressure. J Phys Chem C 125:15301–15315. https://doi.org/10.1021/ACS.JPCC.1C04043/SUPPL_FILE/JP1C04043_SI_001.PDF
45. Bradshaw AM, Hoffmann FM (1978) The chemisorption of carbon monoxide on palladium single crystal surfaces: IR spectroscopic evidence for localised site adsorption. Surf Sci 72:513–535. https://doi.org/10.1016/0039-6028(78)90367-9
46. Oral B, Lee YC, Vook RW (1990) Thermal desorption spectroscopy investigation of CO adsorption on Cu/Pd(111) surfaces. Appl Surf Sci 44:65–73. https://doi.org/10.1016/0169-4332(90)90076-c
47. Carrez S, Dragnea B, Zheng WQ et al (1999) Site selective probe of the desorption of CO from pd(111) by sum frequency generation and fourier transform IR: a comparison of thermal and laser desorption. Surf Sci 440:151–162. https://doi.org/10.1016/s0039-6028(99)00781-5
48. Hoffmann FM (1983) Infrared reflection-absorption spectroscopy of adsorbed molecules. Surf Sci Rep 3:107–192. https://doi.org/10.1016/0167-5729(83)90001-8
49. Lexow M, Maier F, Steinrück H-P (2020) Ultrathin ionic liquid films on metal surfaces: adsorption, growth, stability and exchange phenomena. Adv Phys X 5:1761266. https://doi.org/10.1080/23746149.2020.1761266
50. Massicot S, Sasaki T, Lexow M et al (2021) Adsorption, Wetting, Growth, and Thermal Stability of the Protic Ionic Liquid Diethylmethylammonium Trifluoromethanesulfonate on Ag(111) and au(111). Langmuir 37:11552–11560. https://doi.org/10.1021/acs.langmuir.1c01823
51. Lexow M, Heller BSJ, Maier F, Steinrück HP (2018) Anion Exchange at the Liquid/Solid interface of ultrathin Ionic Liquid Films on Ag(111). ChemPhysChem 19:2978–2984. https://doi.org/10.1002/cphc.201800773
52. Sobota M, Schmid M, Happel M et al (2010) Ionic liquid based model catalysis: interaction of [BMIM][Tf2N] with pd nanoparticles supported on an ordered alumina film. Phys Chem Chem Phys 12:10610. https://doi.org/10.1039/c003753b
53. Kuhn WK, Szanyi J, Goodman DW (1992) CO adsorption on pd(111): the effects of temperature and pressure. Surf Sci 274:L611–L618. https://doi.org/10.1016/0039-6028(92)90834-s
54. Ozensoy E, Meier DC, Goodman DW (2002) Polarization Modulation Infrared reflection absorption spectroscopy at elevated pressures: CO adsorption on pd(111) at Atmospheric Pressures. J Phys Chem B 106:9367–9371. https://doi.org/10.1021/jp020519c
55. Loffreda D, Simon D, Sautet P (1999) Dependence of stretching frequency on surface coverage and adsorbate-adsorbate interactions: a density-functional theory approach of CO on pd(111). Surf Sci 425:68–80. https://doi.org/10.1016/S0039-6028(99)00186-7
56. Kung KY, Chen P, Wei F et al (2000) Sum-frequency generation spectroscopic study of CO adsorption and dissociation on pt(111) at high pressure and temperature. Surf Sci 463:L627–L633. https://doi.org/10.1016/s0039-6028(00)00639-7
57. Bhattacharjee S, Khan S (2020) The wetting behavior of aqueous imidazolium based ionic liquids: a molecular dynamics study. Phys Chem Chem Phys 22:8595–8605. https://doi.org/10.1039/d0cp00143k
58. Wang Z, Li H, Atkin R, Priest C (2016) Influence of Water on the Interfacial nanostructure and wetting of [Rmim][NTf_2] ionic liquids at Mica Surfaces. Langmuir 32:8818–8825. https://doi.org/10.1021/acs.langmuir.6b01790
59. Syres KL, Jones RG (2015) Adsorption, Desorption, and reaction of 1-Octyl-3-methylimidazolium Tetrafluoroborate, [C 8 C 1 Im][BF 4], Ionic Liquid Multilayers on Cu(111). Langmuir 31:9799–9808. https://doi.org/10.1021/acs.langmuir.5b02932